



HAL
open science

Effect of Ti addition on the structural, thermodynamic, and elastic properties of $Tix (HfNbTaZr)(1-x)/4$ alloys

Asif Iqbal Bhatti, Marwa Al-Houcine, Sylvain Queyreau, David Tingaud

► To cite this version:

Asif Iqbal Bhatti, Marwa Al-Houcine, Sylvain Queyreau, David Tingaud. Effect of Ti addition on the structural, thermodynamic, and elastic properties of $Tix (HfNbTaZr)(1-x)/4$ alloys. 2022. hal-03911775v1

HAL Id: hal-03911775

<https://hal.science/hal-03911775v1>

Preprint submitted on 23 Dec 2022 (v1), last revised 21 Jun 2024 (v2)

HAL is a multi-disciplinary open access archive for the deposit and dissemination of scientific research documents, whether they are published or not. The documents may come from teaching and research institutions in France or abroad, or from public or private research centers.

L'archive ouverte pluridisciplinaire **HAL**, est destinée au dépôt et à la diffusion de documents scientifiques de niveau recherche, publiés ou non, émanant des établissements d'enseignement et de recherche français ou étrangers, des laboratoires publics ou privés.



Distributed under a Creative Commons Attribution 4.0 International License

Effect of Ti addition on the structural, thermodynamic, and elastic properties of $\text{Ti}_x(\text{HfNbTaZr})_{(1-x)/4}$ alloys

Asif Iqbal Bhatti ^a, Marwa Al-Houcine ^a, Sylvain Queyreau ^a, David Tingaud ^a

^a Université Sorbonne Paris Nord , Laboratoire des Sciences des Procédés et des Matériaux, LSPM, CNRS, UPR 3407, 99 avenue Jean-Baptiste Clément, F-93430 Villetaneuse, France

Abstract

The structure and thermodynamic properties of $\text{Ti}_x(\text{HfNbTaZr})_{(1-x)/4}$ refractory high entropy multicomponent alloys have been studied using a comprehensive Monte-Carlo Special Quasi-random Structure (MCSQS) realization of the disordered atomic structure and DFT calculations. We have shown that to model the random structure in a small supercell, it is necessary to study a large space of random configurations with respect to the nearest shells. Mimicking the randomness with the many-body terms does not lead to significant improvements in the formation energy but modeling the random structure with the few nearest neighbor pairs leads to improvements in the formation energy. We have also demonstrated the existence of weak to intermediate SRO for equimolar compositions. Chemical ordering is studied by linking a large number of MCSQS realizations to DFT calculations, and the SRO results are rationalized in terms of the crystallographic structure of the element pairs and binary phase diagrams. The formation energy of $\text{Ti}_x(\text{HfNbTaZr})_{(1-x)/4}$ alloys remains slightly positive for all x when Ti is added. For $x > 0.5$, a phase transition in favor of an hcp structure is observed in agreement with the Bo-Md diagram. A dual phase is predicted at $x = 0.5$. The Ti content in this class of alloys appears to be a practical way to select the phase structure and tailor the structure and elastic properties to specific applications.

Keywords: High entropy alloys, Random alloys, Special Quasi-Random structures (SQSs), Density Functional Theory (DFT), Configurational entropy, Phase stability, Body-centered cubic (bcc).

1 Introduction

In recent decades, Ti alloys have made great progress in the application of biomaterials that are not only environmentally friendly but also less toxic and compatible with bone tissue [1]. Ti-based alloys have been used for orthopedic and dental implants due to their high corrosion resistance but suffer from fatigue stresses and metal wear due to their high elastic modulus. Over time, these stresses lead to inflammation and subsequent damage to bone tissue. Elastic properties are particularly interesting for biological applications, as Young's modulus compatibility with bone is critical. Therefore, recent research has focused on the development of new Ti-based alloys with a lower modulus of elasticity [2].

Refractory High-Entropy Alloys (RHEAs) exhibit unique properties such as a high density, nontoxicity, which make them more compatible with the biological environment, and mechanical properties that exceed those of Ti-based alloys, making them particularly attractive for the associated applications [3]. These HEAs are typically composed of four or more elements at nearly the same concentration [4–6]. Despite consisting of a complex multicomponent system, they lead to the formation of a simple single-phase solid solution, such as face-centered cubic (fcc), body-centered cubic (bcc), or hexagonal close-packed (hcp). Among these alloys, fcc HEAs have been widely studied, but few studies exist on bcc HEAs, and even fewer in the case of bcc refractory HEAs (RHEAs) [7,8].

Recent experiments on TiTaHfNb, TiTaHfNbZr, and TiTaHfMoZr have shown that the non-toxic and non-allergenic elements such as Nb, Ta, and Zr have high corrosion resistance [9]. Properties such as high ductility, corrosion resistance, and strength at both room and high temperatures can be improved by choosing suitable refractory elements (a mixture of bcc and hcp elements).

As for the phase stability of the quaternary alloy (HfNbTaZr), as-cast experiments have shown that this structure exists as a bcc structure with a reported lattice parameter of 3.446 Å [10]. However, a recent experiment by Huang *et al.* showed that cold rolling and annealing of this alloy produces a two-phase structure [11] Therefore, they did not investigate the structural properties due to poor malleability.

Much of the properties of HEA such as formation energies or dislocation kinetics are rooted in the atomic structure of these alloys, that may well deviate from the ideal random structure. However, in absence of direct experimental observations at the lattice length scale, chemical ordering is mostly unknown and remain a challenging task to simulation approaches. For medium to high entropy alloys, short-range order (SRO) effect has been investigated in bcc and fcc HEAs [12–16]. Tamm *et al.* [17] showed for a NiCrCo medium entropy alloy the existence of SRO decreases the configurational entropy and affects the formation energy of the system [18]. Likewise, Yin *et al.* [12] have shown using Monte-Carlo (MC) and DFT calculations that quaternary MoNbTaW alloys exhibit an SRO.

In this paper, our objective is to systematically investigate the effects of Ti content on the atomic structure, phase stability, chemical local ordering and elastic constants using MCSQS and DFT calculations. The results regarding dislocation structure and properties, that control

the plastic behavior and forming capability of this system are left for an upcoming paper [Asif Iqbal *et al.* to be published 2023]. The paper is organized as follows: Section 2 explains the methods and techniques used to compute the random supercell. Section 3 provides results and discussion, and the last section summarizes the conclusions.

2 Methodology and Computational details

In the present article, we report the formation energy, elastic properties and structural parameters of a model of the $\text{Ti}_x(\text{HfNbTaZr})_{(1-x)/4}$ alloys calculated using Density Functional Theory (DFT) as implemented in Vienna ab initio simulation (VASP) code [19]. The Projector Augmented Wave (PAW) pseudopotential was used to approximate the electron core energy [20] and the Perdew-Burke-Ernzerhof (PBE) generalized gradient approximation was used to approximate the exchange correlation functional (XC) [21]. The plane-wave cut-off energy was set to 600 eV. The first order Methfessel-Paxton method [22] with a smearing parameter of 0.2 eV was used. Brillouin zone integrations were performed with Γ -centered k-points mesh generated by the Monkhorst-Pack (MP) method [23].

Construction of a $\text{Ti}_x(\text{HfNbTaZr})_{(1-x)/4}$ supercell

A lot of care has been paid to the construction of the disordered structure corresponding to the $\text{Ti}_x(\text{HfNbTaZr})_{(1-x)/4}$ alloys. The composition was varied from $x = 0.0$ to 0.81, by steps of 0.1, while the rest of the composition is equally distributed among other elements Hf, Nb, Ta, Zr. For all considered compositions, the supercell geometry was constrained so that the cubic bcc symmetry was preserved as experiments suggest that most compositions correspond to a bcc single phase. Additional calculations using an hcp or orthorhombic lattice have also been conducted. Mimicking a random structure in a supercell of sufficiently limited dimensions to be tractable by DFT simulations, raises an additional problem arising from the short-range spatial correlations among atoms induced by the Periodic Boundary Conditions (PBC). To overcome this issue, several techniques have been proposed in the literature and they rely on the usage of order parameters to assess the disordered nature of the atomic configuration and the minimization of the spatial correlations as much as possible [24–28]. Here, we choose to use the Monte-Carlo Special Quasi-random Structure (MCSQS) technique implemented in the Alloy Theoretic Automated Toolkit (ATAT) code [29,30] to generate a random structure in a small periodic supercell. Hence, it allows us to perform a statistical study of the MCSQS parameters on the resulting structure of different atomic configurations.

The supercell size was chosen to be a necessary tradeoff between physical relevance and numerical cost of the calculations. The supercell geometries depend on the investigated composition and are as follows. For $x = 0.11, 0.33, 0.4, 0.63,$ and 0.70 , we generated a supercell of 54 atoms based on $3 \times 3 \times 3$ cubic bcc unit cells; for compositions corresponding to $x = 0.0, 0.50,$ and 0.81 , a supercell of 128 atoms based on $4 \times 4 \times 4$ cubic bcc unit cells was used; and for $x = 0.20$, a supercell of 125 atoms based on $5 \times 5 \times 5$ primitive bcc unit cells was used. In the case of hcp structures, we employed supercells of 128 atoms for $x = 0.5, 0.81$ ($4 \times 4 \times 4$ hexagonal unit cells) and 54 atoms for $x = 0.63, 0.70$ ($3 \times 3 \times 3$ hexagonal unit cells).

In all the reported simulations, the system was allowed to fully relax, including atomic positions and the supercell dimensions (in an anisotropic fashion) using a conjugate gradient algorithm. The system was assumed to have converged when the force on each atom was less than $1 \text{ meV}/\text{\AA}$, and a stress tolerance below $\sim 0.005 \text{ GPa}$. After relaxation, the formation energy was evaluated from a single point energy calculation with a dense k-point relative to the

convergence of the formation energy. A sensitivity study showed that a tolerance of 1 meV/atom, a $2 \times 2 \times 2$ k-points mesh grid and plane-wave cut-off energy 600 eV were sufficient for the calculation of elastic and structural properties.

3 Results and Discussion

We employed MCSQS approach to mimic the random structure of HEA in a DFT supercell. While MCSQS is now a well-established technique within the HEA community, its results can be impacted by a few parameters, in particular the number of neighbor shells and the order of the many-body terms that are included to evaluate the disorder in the considered configuration. We thus start with a sensitivity study of the structure generated as function of these parameters.

We begin our analysis by calculating the structure and formation energy for each SQS supercell using DFT. Since we have only limited experimental results for all the considered compositions, we will understand the stability of the HEA structure as Ti is introduced into the quaternary alloy. In the present work, we varied the pairwise terms (called hereafter ' p ') among the Nearest Neighbor (NN) shells with p going from 2 to 10 NN. We also varied the three-body terms (t) and four-body terms (q) terms (with t and q going from 0 to 1 NN).

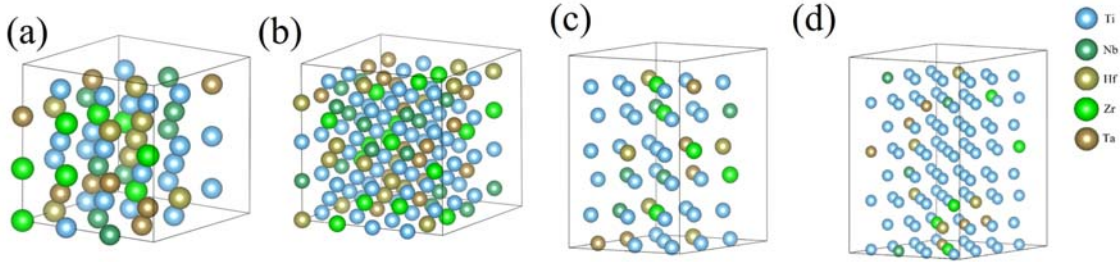


Figure 1: Examples of supercells [(a)-(d)] obtained from MCSQS for the alloy $\text{Ti}_x(\text{HfNbTaZr})_{(1-x)/4}$. Figure (a) and (c) show a $3 \times 3 \times 3$ supercell for $x = 0.12, 0.33, 0.40, 0.60,$ and 0.70 containing 54 atoms with bcc and hcp structure, respectively. Figure (b) and (d) show a $4 \times 4 \times 4$ supercell for $x = 0.0, 0.50,$ and 0.80 representing 128 atoms with a bcc and hcp structure, respectively.

For each Ti content x and MCSQS parameters p , t , and q (hereafter denoted by the value triplet (p, t, q)), about 20 different calculations were performed. **Figure 1** shows some of the atomic configurations resulting from the MCSQS calculations obtained for different Ti content x . Our workflow consists of first generating 20 SQS for $(p, 0, 0)$ only, then with $(p, t, 0)$, and finally (p, t, q) . In each case, the MCSQS calculation was initiated with different random seeds, leading to different final atomic configurations. The final configuration was reached when the local minimum of the objective function was reached during the runtime of 120 hours. MCSQS was terminated earlier when no further SQS structure was generated for more than 12 hours.

According to classical theory, the Gibbs free energy of the system is given by,

$$\Delta G_x = (\Delta H_{\text{form}})_x - (T\Delta S_{\text{conf}})_x - (T\Delta S_{\text{vib}})_x \quad (1)$$

In **Eq. 1**, $(\Delta H_{\text{form}})_x$ is the formation energy and ΔS_{conf} and ΔS_{vib} are the configuration and vibrational entropy terms, respectively. The formation energy, $(\Delta H_{\text{form}})_x$, given in **Eq. 2** is computed from the difference of energy of the SQS supercell and the energy E_i associated to the most stable phase of each elements, i , (bcc for Nb, and Ta and hcp for Hf, Ti, and Zr):

$$(\Delta H_{\text{form}})_x = (E_{\text{SQS}})_x - (\sum_i c_i E_i)_x \quad (2)$$

where c_i is the atomic fraction of an alloy element, i . For alloys, the configurational entropic term is given by,

$$\Delta S_{\text{conf}} = -k_B \sum_i c_i \ln(c_i) \quad (3)$$

where k_B is the Boltzmann constant. It can be noted that **Eq. 3** applies to perfect random solid solutions, which might not be the case of HEA alloys where some level of chemical order may exist in these systems (see later). **Eq. 3** is nevertheless commonly used within the HEA community to estimate the configurational entropy. The last term of **Eq. 1**, corresponding to the vibrational entropy, can be calculated from DFT using the so-called frozen phonon approach [31]. However, these types of calculations are computationally demanding, and vibrational entropy is commonly neglected when compared to the configurational entropy [4,16,27,32]. This last term is thus disregarded in the present study.

3.1 Sensitivity study on MCSQS parameters

First, we conducted MCSQS calculations while neglecting the many-body terms, i.e., we included only the pairwise (p) NN shells as these terms are expected to have the largest impact on the resulting SQS configuration. We then determined the effect of the number of p shells on the formation energy. We have considered $x = 0.33$ composition and assume that similar trends could be obtained for other compositions. **Table 1** shows the formation energy and average lattice parameter as a function of p shells. The values given here refer to the lowest formation energy obtained over 20 different SQS calculations. Interestingly, the formation energy per atom decreases only weakly as the number of p NN shells increases up to 8 NN. When $p = 10$ NN, the MCSQS calculations surprisingly yielded to a larger formation energy per atom by about 7 meV/atom. In the latter case, it is probable that the convergence was not met within the 120-h left for the calculations. As a result of this sensitivity study, we chose $p = 8$ NN as a compromise between MCSQS capacity to produce low energy configuration and the numerical cost to run the MCSQS.

Table 1: Calculated average lattice parameters a' , and formation energy for $x = 0.33$ using a 54-atom supercell over 20 different initial SQS seeds (i) for each value of p along with the average (avg) formation energy value and standard deviation (σ). The number of nearest neighbor (NN) shells is given by the following convention: p NN where p is the nearest neighbor shells for the pair.

$x = 0.33$			
#Shells ($p,0,0$) NN	$\min_i\{\Delta H_i\}$ meV/atom	avg $\pm\sigma$	a' Å
2	84.73	88.56 \pm 3.2	3.382
4	82.37	89.05 \pm 3.9	3.384
6	81.27	89.70 \pm 3.6	3.383
8	80.37	86.80 \pm 3.8	3.383
10	87.30	90.49 \pm 2.6	3.382

In another set of calculations, we have investigated the possible effect of higher order many-body terms: ternary (t) and quaternary (q) interaction within 1st NN shells from MCSQS. For this, many-body terms were set to $t = 1$ NN, and $q = 0$ or 1 NN, while the pairwise terms were set to 6 and 8 NN shells.

Figure 2 shows the impact of including higher order many-body terms on the formation energy of $Ti_x(HfNbTaZr)_{(1-x)/4}$ for each Ti content x . The figure reports the Average (avg) formation energy value, along with the standard deviation (σ) and minimum and maximum energy values. Overall, it is clear that average formation energy decreases as Ti_x content increases. For a given Ti_x and triplet (p, t, q) , the formation energy shows a rather large scatter with variations of up to about 20% depending on the initial seed values used in the MCSQS calculation. The scatter observed among the 20 realizations seems to depend upon the x content and the supercell size. This could be investigated further.

Further, the average formation energy over 20 initial seeds is weakly impacted when three and four body terms are included. For a given Ti content x , the average formation energy (shown in blue color) decreases only weakly when including t , and q terms, except for $x = 0.40$, for which the energy varies by about ~ 4 meV/atom (corresponding to triplet (8,0,1)). A similar conclusion was also reached by Tian *et al.* [33] for CoCrFeMnNi, Ta-W, and CoCrNi alloys. Using the Similar Atomic Environment (SAE) approach, these authors showed that including many-body clusters did not provide much improvement in the cross-validation error between SAE and SQS, implying that pair NN terms for atom pairs is sufficient to model a random structure [33].

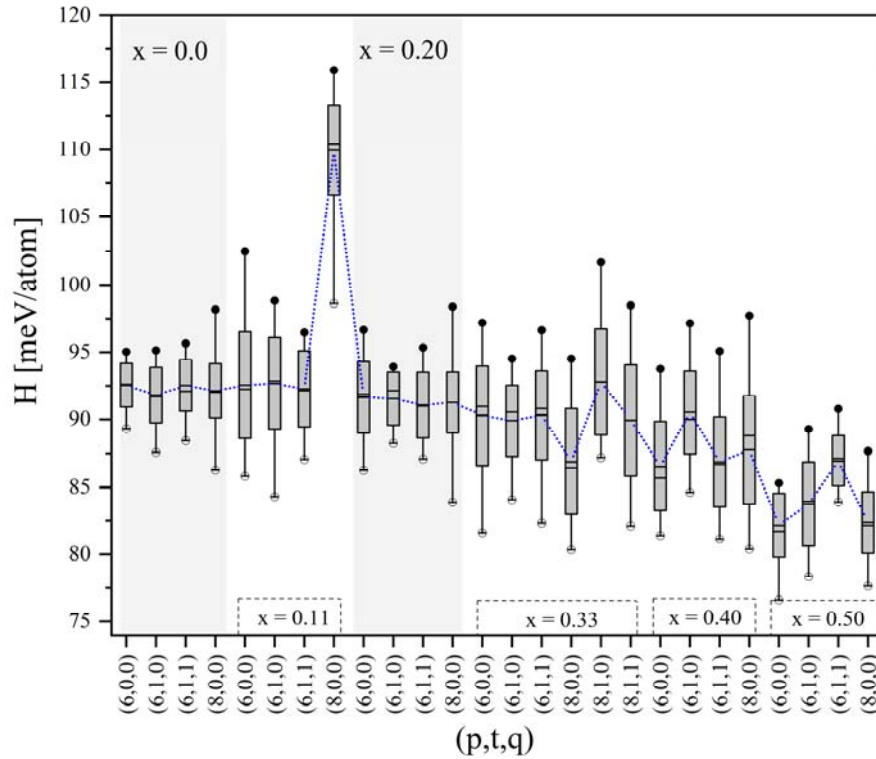


Figure 2: Statistical plot showing the average, minimal, maximal values and the standard deviation of the calculated formation energy for $\text{Ti}_x(\text{HfNbTaZr})_{(1-x)/4}$ alloys. The number of shells is given by the following convention: (p, t, q), where p, t, q are the pair, three-body, and four-body terms, respectively. Maximum values are represented by black filled circles and minimum values by empty circles. The average formation energy for each composition is shown in blue color.

In summary, this sensitivity study performed over 480 different calculations demonstrates the importance of performing multiple MCSQS calculations with different initial seeds to evaluate the statistical differences that result from the MCSQS calculations. The inclusion of a large number of NN shells for pair interactions has an important impact on the ability of the SQS to yield lower energy configurations. For $p = 8$ NN shells, we found a practical optimum for $x = 0.0, 0.20, 0.33,$ and 0.40 in the present case. The inclusion of ternary and quaternary interaction terms up to 1 NN shell appears to have only a second-order effect in the present system.

For the analyses that follow, we will consider the atomic configuration corresponding to the system with the lowest energy for each x as the most thermodynamically probable.

3.2 Analysis of the Chemical short-range order of the bcc phase

The results of previous section, raise the question of whether the final configuration among all SQS structures exhibit a local chemical order, i.e., whether the favorable pairings between elements are preferred leading to a configuration with the lowest formation energy? To investigate SRO, Yin *et al.* and collaborator [18] employed MC and DFT to minimize the energy in a bcc HEA system. As a less computationally demanding approach, we propose to sample the energy of a disordered atomic configuration making use of a large number of different SQS simulations. We chose the equimolar case $x = 0.0$ and 0.20 and generated another 650 SQS structures using our optimized SQS parameters ($p=8, t=0, q=0$) NN pairs. SQS calculations were run to produce a random structure in maximizing the objective function using the same convergence criterium as above. After this, relaxation of each structure was done using DFT and the formation energy was evaluated for all 650 different initial configurations. To quantify the short-range order (SRO) in these simulations, we use the SRO parameter α_{ij} described by Fontaine *et al.* [34],

$$\alpha_{ij} = ((n_j / m_A) - c_j) / \delta_{ij} - c_j \quad (4)$$

Here, i refers to the reference atom. n_j is the number of atoms of the non-reference type among the c_j atoms in the i -th coordination shell. m_A is the concentration of the non-reference atom. If $i = j$, $\delta_{ij} = 1$, otherwise the Warren-Cowley SRO parameter is returned. The total SRO, $\sum_{ij} |\alpha_{ij}|$, is calculated by summing all pairwise terms around the reference atom in the bcc structure for the first two and three nearest neighbor coordination shells (2 NN and 3 NN), respectively. We employed the tool developed in [35] and extended it to perform the analysis including the first three nearest neighbor coordination shells (3NN). In **Figure 2**, for $x = 0.0$ and 0.20 , the low and high formation energy of the configurations are shown along with the standard deviation and average values.

To assess the SRO, we sort the different atomic structures with respect to the simulated energy configuration. First, we checked the meaning of this sorting by analyzing the average over all 650 different configurations. Thus, a first set of data corresponds to the average over all data and is shown as green curves in the **Figure 3, 4 and 5**. As desired, the SRO parameter is close to zero for all pair types. A small deviation on the SRO parameter of 0.01 is found on this average, and this gives an estimate of the precision we can expect from our analysis. The fact that the SRO parameter is very close to zero means that the average of all 650 SQS configurations is a good approximation of the ideal random solid solution. This neutral curve is considered as a reference value for the next steps. Two bins were then considered: The configurations with the lowest energy are grouped and called the best set, while the configurations with the highest energy are called the worst set. To determine the SRO for the best SQS, we averaged the SRO values of each pair type for a group of "best" cases with the lowest energy and used the same strategy for the worst SQS. We varied the size of these bins from 6 to 65 configurations (1-10% of the total data) and a larger bin size smooths the results by reducing the obtained averaged SRO parameter values. However, the sign of the SRO parameters, indicating whether a binding type is more or less present than in the ideal random structure, remained largely unchanged when the bin size was varied.

3.2.1. SRO in the quaternary HfNbTaZr system

Before comparing the results of our two compositions, **Figure 3** shows the radar plot for $x = 0$ and $x = 0.2$, and the analysis is admittedly not straightforward. This analysis was performed for the first 2 NN shells, where most of the SRO can be observed. An SRO parameter with a negative sign indicates a pair type that is more abundant in the atomic structure under consideration than in the ideal random configuration. When comparing two different SQS realizations, an increase in formation energy can be explained in two ways: a lower representation of favorable pair types and/or an increase in the contribution of unfavorable atomic pairs. Comparing the results for the best and worst sets, we see that the SRO data for the two sets agree well, i.e., favorable bonds are found in greater numbers in the best sets ($a_{ij} < 0$) and unfavorable bond types in smaller numbers ($a_{ij} > 0$). However, the trend is less clear when the SRO parameter is close to zero, indicating a neutral influence of the corresponding pair.

Turning now to the specifics of interactions in quaternary alloys, of the 10 different bond types, the following pairs appear to be favorable (in decreasing order): Nb-Ta and Hf-Zr; the same atom pairs (e.g., Hf-Hf) show a nearly neutral interaction ($a_{ij} = 0$); finally, the last pair types seem to be unfavorable (in decreasing order): Hf-Nb, Ta-Zr, Nb-Zr, and finally Hf-Ta. Interestingly, the classification of a bond 'ij' can also be determined in a completely different way, namely by a linear fit of the configurational energy as a function of the parameter set a_{ij} calculated for all 650 SQS realizations, where favorable (or unfavorable) bonds are associated with a negative slope (positive) of the linear fit. This further strengthens the confidence in the proposed SRO analysis.

Previous results strikingly indicate a simple correlation between the favorable nature of the bond types and the crystallographic reference structure of the two elements involved in the pair

type. This is shown in **Figure 4(a)**, where an SRO parameter is defined as the sum of SRO values corresponding to pairs of elements depending on their structure: bcc-bcc, hcp-hcp, or bcc-hcp elements (at 0 K). Elements with identical reference crystallographic structure clearly seem to lead to favorable bonds associated with a decrease in formation energy, while those with different bcc-hcp crystallographic structure are clearly unfavorable. It would be interesting to nuance this rather simple sorting of SRO analysis by combining our SRO results with analysis of the binary phase diagrams of the elements that make up our system. This is reserved for a later study. **Figure 5(a)** shows the SRO parameter a_{ij} when performing the analysis of an increasing number of shells from 1 to 3 NN shells for the best SQS realizations. Interestingly, the first NN shell is associated with rather weak SRO parameters for all bond types, so that the chemical SRO is limited to the 2nd and 3rd NN shells, which have a larger number of atomic layers. In this system, the SRO parameter values for the 2nd and 3rd NN shells are meaningfully the same, indicating that most of the SRO occurs in the 2nd NN shell.

3.2.2. SRO in the HfNbTaTiZr system and comparison between the two systems

Turning now to the quinary system, some of the previous observations can be repeated, although the details may differ. **Figure 3(b)** shows that the average SRO parameters for all 15 bond types are close to zero for all 650 SQS realizations, consistent with the ideal random solid solution. The best and worst data points again complement each other well, with some exceptions that we will discuss later. The following bond types appear to be uniquely favorable in this new system ($a_{ij} < 0$ for the best set): Hf-Zr, Hf-Ti, Nb-Ta; the same element pairs 'i-i' are typically neutral ($a_{ij} = 0$), while the following bonds appear unfavorable ($a_{ij} > 0$): Hf-Ta, Nb-Ti, Nb-Zr, Ta-Zr. The results for some bond pairs such as Ta-Ti, Ti-Ti are less clear. Perhaps more SQS realizations are needed to analyze this more complex quinary system.

The simple sorting of bond types as a function of the crystallographic structure of each element is shown in **Figure 4(b)**. As with the quaternary alloy, the sum of the SRO parameters is favorable for pairs of elements with the same bcc-bcc or hcp-hcp structures, although the SRO parameter for hcp-hcp has a lower value here. The SRO parameter for bcc-hcp element bonds is unfavorable and has a much larger value than in the quaternary system. Finally, the SRO parameters for all 15 pair types are analyzed as a function of NN shells and shown in **Figure 5(b)**. In the quinary system, the bond types are polarized even in the 1st NN shell, where the SRO value closely follows the sorting by the crystallographic nature of the elements involved in the bond (the agreement is better than when considering 1+2NN shells). The SRO data for other shells typically evolve uniformly from this 1st NN shell to the following 2nd and 3rd NN shells. Thus, the chemical order in the quinary system appears to be more complex and comprehensive than in the quaternary systems, as the 1st, 2nd, and 3rd NN shells exhibit SRO.

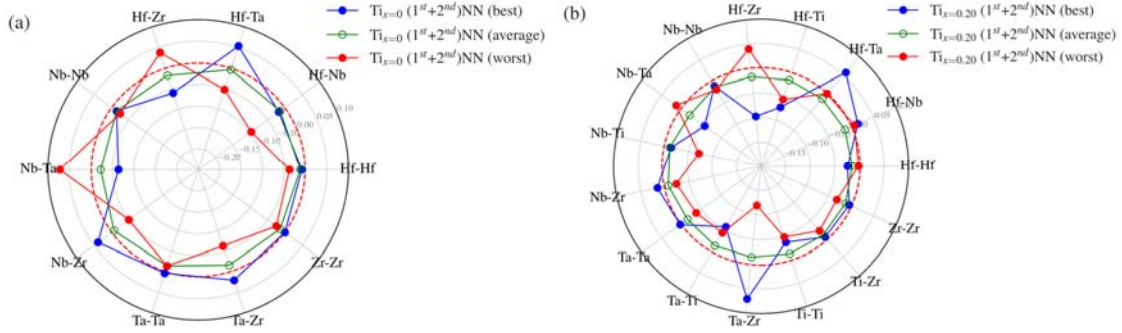


Figure 3: Radar plot showing the average, best (average over fifteen datapoints), and worst (average over fifteen datapoints) case for the 1st + 2nd (2NN) data points for (a) $x = 0$ and (b) $x = 0.20$, respectively. The best and worst SQS is an average over fifteen data points. "Average" here refers to the average over all data points. The ideal random solid solution is represented by the dashed red line.

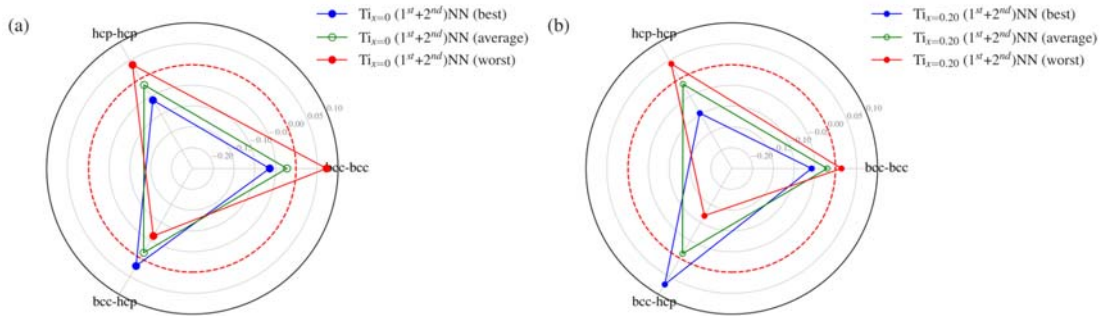


Figure 4: Radar plot showing the average, best (average over fifteen datapoints), and worst (average over fifteen datapoints) case for the 1st + 2nd (2NN) data points for (a) $x = 0$ and (b) $x = 0.20$, respectively. The best and worst SQS is an average over fifteen data points for selected bcc-bcc, bcc-hcp, and hcp-hcp phases. "Average" here refers to the average over all data points. The ideal random solid solution is represented by the dashed red line.

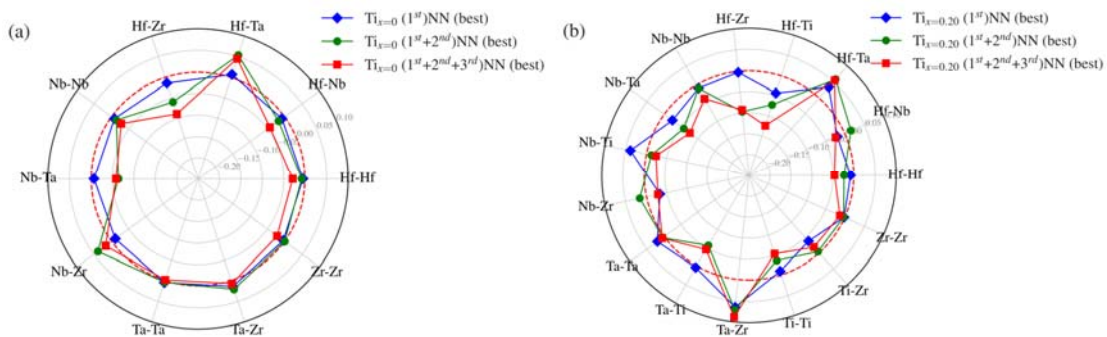


Figure 5: Radar plot showing the best SQS realizations for the 1st (1NN), 1st + 2nd (2NN), and 1st+2nd+3rd (3NN) shells for two systems (a) HfNbTaZr and (b) HfNbTaTiZr, respectively. The best SQS is an average over fifteen data points. The ideal random solid solution is represented by the dashed red line.

The total SROs for $x = 0.0$ and 0.20 are given in **Table 2** and are calculated from the sum of the first two and the sum of the first three nearest neighbor (NN) shells. In our analysis, we find that for $x=0$, we have the lowest SRO value for the lowest energy configuration compared to the highest energy configuration. For $x = 0.20$, the SRO values are higher for the configurations with the lowest energy, indicating the existence of SRO. When comparing the quaternary and quinary alloys, the SRO in the first system is mostly localized on the 2nd NN shell and only two bond types (Nb-Ta and Hf-Zr) are favorable, four bond types are unfavorable and same element bonds are mostly neutral. In the quinary system, four bond types are favorable, 6 types are unfavorable, and 5 types are mostly neutral, while the chemical ordering covers at least all 3 NN shells. Since, in a finite sized supercell, the bond type contributions are related through the imposed overall alloy composition, the quaternary system seems more constrained, and this could explain why the total SRO is smaller in that system. In the study performed by Yin *et al.* using the Monte Carlo approach (MC), the author observed a large Warren-Cowley SRO value (in the range of 1.75-2.00) for bcc MoNbTaW RHEA for the lowest energy configuration considering only the first 2NN shells [18]. However, it should be noted that the quaternary system they studied is arguably simpler as it consists of only bcc elements. For alloys consisting of bcc and hcp elements, the local ordering appears thus to be complex. The chemical ordering observed in our systems could therefore be responsible for the apparent metastability of the bcc phase deduced from our simulations.

Table 2: Total SRO of the lowest and highest energy SQS configurations for the combined 1st+2nd nearest neighbors (2NN) and 1st+2nd+3rd nearest neighbors (3NN) shells, respectively. Total SRO is determined by using $SRO = \sum_{ij} |\alpha_{ij}|$.

$Ti_x(HfNbTaZr)_{(1-x)/4}$	2NN	3NN	2NN	3NN
x	low		high	
0.0	0.57	0.51	0.88	0.82
0.2	1.55	1.61	1.46	1.48

3.3. Possible phases according to the Bo-Md diagram

To predict the phase stability in our alloys, we reprise the d -electrons theory initially proposed to predict the phase stability of Ti-based alloys. Morinaga *et al.* originally proposed this theory to classify Ti based alloys into α or $\alpha+\beta$ or γ phase as function of solely two parameters: Bo and Md [36]. Bo is the bond strength between the Ti and the alloying elements with $Bo \leq 2.84$, and Md is the metal's d-orbital energy level, which corresponds to element's metallic radius and electronegativity [36]. Based on this, Hadi *et al.*, extended the single β -phase field to the domain where $Bo \leq 2.96$. With this extension the authors showed that the inclusion of Al, O, and Sn increased the stability of the β -phase [37].

For typical Ti based alloys these parameters are given as composition averages $\overline{Bo} = \sum c_i Bo_i$ and $\overline{Md} = \sum c_i Md_i$. The c_i is the concentration of the alloying elements. **Table 3** lists the composition averages for the alloys considered here. The reference Bo and Md values for each element in bcc Ti is taken from Hadi *et al.* [37]. We will assume that this analysis is still valid for our alloys, in which Ti is not the main constituent in some of our nuances. A similar assumption was made in another DFT study [38], and we will see later that the predictions from Bo-Md diagram agree well with our DFT data.

Table 3: The \overline{Bo} and \overline{Md} for the $Ti_x(HfNbTaZr)_{(1-x)/4}$ alloys are calculated using the reference values of Bo and Md from Hadi *et al.* [37].

x	0.0	0.11	0.20	0.33	0.40	0.50	0.63	0.70	0.81
\overline{Bo}	3.11	3.074	3.046	3.003	2.979	2.95	2.908	2.884	2.850
\overline{Md}	2.715	2.685	2.662	2.626	2.607	2.582	2.548	2.528	2.499

In the $\overline{Bo} - \overline{Md}$ diagram shown in **Figure 6**, the domain of stability associated to the various possible phases of Ti based alloys are drawn along with some examples from the literature [37,38]. The solid line in red is extrapolated for $Ti_x(HfNbTaZr)_{(1-x)/4}$ alloys with the composition studied in the present work to pure Ti system. For compositions well above the dashed line in the $\overline{Bo} - \overline{Md}$ diagram, a bcc structure is expected, while for compositions well below the same line structures tends to become hcp. Close to the border, bcc, hcp and orthorhombic structures are all possible and may be metastable. From this, we thus expect the decrease of formation energy and stable phase change from bcc to hcp when increasing the Ti content from $x = 0$ to $x = 0.81$ in our alloys. For $x = 0.0$ (the quaternary alloy without Ti and $x = 0.2$ (the equimolar case), experimental studies exist and provide clear reference data in the shape of unambiguous identification of a single HEA phase of bcc structure [11,39], corresponding to well defined X-ray diffraction peaks for the bcc structure. The $\overline{Bo} - \overline{Md}$ diagram predictions are thus in agreement with these studies on HEA alloys. From this, it becomes clear that relevant MCSQS and DFT simulations must provide not only for the bcc phase but also for the hcp phase at larger Ti content x .

3.4. Structure and stability of the bcc phase as function of the Ti content

In this section, we present DFT results on the effects of Ti content on the structure and relative stability of the possible HEA phases. For $x = 0.0$ and $x = 0.2$, there are experimental studies that provide clear reference data for the identification of a single bcc phase [11,39]. Unfortunately, there are no experimental or theoretical data for x other than 0.0 and 0.2 with which to compare our results.

Table 4 shows the structural parameters for the configurations corresponding to the lowest formation energy. The relaxed lattice parameters (a , b , c) deviates slightly from the perfect bcc lattice. They are slightly anisotropic (with an average difference of about 3%), and the angles (α , β , γ) between basis vectors of the supercell slightly differs from the expected 90 deg (by typically less than 1 deg). These small distortions are unsurprising for HEA systems, as differences in the local chemical order are expected along the supercell axis especially for the small dimensions dealt with in DFT.

The average lattice parameter $a' = (a+b+c)/3$ decreases from 3.436 Å to 3.306 Å with the increase of Ti content from 0.0 to 0.81 assuming the alloys preserve a bcc phase highlighted in **Table 4**. From experiments, it is known at temperature above 1100 K, the hcp elements transition to the bcc phase. The reported lattice parameters in the bcc phase are $a_{Ti} = 3.306$ Å, $a_{Zr} = 3.609$ Å, and $a_{Hf} = 3.651$ Å at temperatures 1155 K, 1140K and 2016 K, respectively [40,41]. To compare our results with the bcc lattice parameters, the lattice parameters are extrapolated to room temperature (RT) by using the thermal expansion coefficients for the bcc elements Hf, Zr, Ti given in reference [42,43]. The so calculated bcc lattice parameters for the elements are $a_{Ti} = 3.276$ Å, $a_{Hf} = 3.559$ Å, and $a_{Zr} = 3.582$ Å. Thus, the lattice parameters a_{Ti} fall within the range of $x = 0.81$. Finally, the DFT calculations reproduce well the experimental values for $x = 0$ and $x = 0.2$, which gives confidence in our methodology relying on several sets of MCSQS and DFT simulation conditions.

The known stable experimental lattice parameters at RT for stable elements are $a_{Ti} = 2.95$ Å, $c/a_{Ti} = 1.58$ Å, $a_{Zr} = 3.23$ Å, $c/a_{Zr} = 1.59$ Å, $a_{Hf} = 3.196$ Å, $c/a_{Hf} = 1.58$ Å, $a_{Nb} = 3.30$ Å, and $a_{Ta} = 3.31$ Å. The lattice constants for pure Ti (hcp) unit cell are $a = b = 2.950$ Å and $c = 4.687$ Å [39]. For large Ti content typically $x = 0.5$ and above, the $\overline{Bo} - \overline{Md}$ diagram suggests that hcp and/or orthorhombic (ortho) structure may be stable. We thus performed another set of MCSQS+DFT calculations for these crystallographic structures. The same methodology as discussed in the previous **section 2** was adopted. To assess the prediction of the $\overline{Bo} - \overline{Md}$ diagram, we generated a set of MCSQS structure assuming the hcp phase for x ranging from 0.5 to 0.81. At $x = 0.5$, other phases could exist near the extrapolated red line (shown in **Figure 6**); therefore, we have generated additional SQS structure with orthorhombic symmetry. In all cases, twenty different SQS structures were obtained and compared to select the one associated to lowest formation energy.

The bottom of **Table 4** (hcp and ortho) shows the lattice geometry obtained for these simulations. The simulated lattices are again slightly distorted when compared to a perfect hcp lattice, certainly because the different element arrangements are probed along the supercell

axis. Surprisingly, no clear trend was found regarding the evolution of the average a and c/a ratio in the case of the hcp structure as the Ti content increases.

Table 4: Detailed analysis of the structure of the atomic configurations after relaxation for $\text{Ti}_x(\text{HfNbTaZr})_{(1-x)/4}$ alloys as function of the Ti content x , and the choice of crystallographic structure. The average lattice parameters a' are reported for the conventional unit cell. The number of atoms is given for the SQS supercell generated from MCSQS. Known experimental values are reported from [11,39] and are given in parentheses.

Phase	x	#atoms	\AA			α	β	γ	a'
			a	b	c				
bcc	0.00	128	3.454	3.417	3.438	89.6	90.0	90.0	3.436(3.446)
	0.11	54	3.429	3.408	3.425	89.5	89.8	89.9	3.420
	0.20	125	3.398	3.417	3.405	89.7	89.6	89.8	3.407(3.404)
	0.33	54	3.392	3.372	3.381	89.7	90.1	89.9	3.381
	0.40	54	3.371	3.336	3.403	89.5	89.9	89.6	3.370
	0.50	128	3.379	3.321	3.361	89.9	90.8	90.0	3.353
	0.63	54	3.313	3.345	3.339	90.6	88.6	90.7	3.332
	0.70	54	3.300	3.305	3.350	89.2	90.4	90.5	3.318
	0.81	128	3.073	3.421	3.418	85.8	89.9	90.1	3.306
ortho	0.50	32	3.402	3.243	4.674	89.2	90.3	89.3	
hcp	0.50	128	2.933	2.942	4.680	90.1	89.7	110.9	$a=2.937,$ $c/a=1.593$
	0.63	54	3.318	2.961	4.543	89.9	90.0	123.8	$a=3.319,$ $c/a=1.447$
	0.70	54	2.953	3.285	4.533	89.7	89.6	123.7	$a=3.119,$ $c/a=1.453$
	0.81	128	2.934	2.997	4.687	90.0	89.9	119.3	$a=2.963,$ $c/a=1.580$

We now consider **Figure 4(a)** where the calculated formation energies of the possible phases of $\text{Ti}_x(\text{HfNbTaZr})_{(1-x)/4}$ are plotted as function of the Ti content. Formation energies are calculated using **Eq 2** by taking the most stable phase of the alloying elements as a reference. Interestingly, the formation energies of all phases of the alloy are slightly positive for all Ti content. The corresponding values are however small, below 100 meV/atom, while their counterparts for pure elements are of the order of few eV/atoms.

The formation energy of the bcc phase is found to decrease monotonically with Ti content. For $x = 0.20$, which corresponds to the equimolar case, the formation energy of 84.4 meV/atom

determined in the present study is almost 2 meV/atom lower than the DFT calculations of Gao *et al.* [44], where a value of 86.5 meV/atom was reported. This is because we used the large configuration space and were able to find the configuration corresponding to the structure with the lowest energy.

If we compare the relative stability of the possible phases for $x > 0.5$ in **Figure 4(a)**, formation energy for the hcp phase becomes lower than that of the bcc phase and decreases faster as Ti content is increased. This suggests that alloys with large Ti content may exhibit an hcp structure or a dual bcc and hcp phase, since the difference between the two structures is small (typically below 7%). Finally, the formation energy of the orthorhombic phase at $x = 0.5$ is larger than that of the bcc and hcp phases. The difference between bcc and hcp is about 2 meV/atom and between bcc and ortho about 8 meV/atom.

Figure 4(a) also displays the formation energies of pure Ti in bcc and hcp phases as an asymptotic behavior for the $\text{Ti}_x(\text{HfNbTaZr})_{(1-x)/4}$ alloy as x tends to 1. The formation energy of our $\text{Ti}_x(\text{HfNbTaZr})_{(1-x)/4}$ alloys in the hcp structure smoothly decreases towards the one of pure Ti in hcp structure.

To set the formation energies of **Figure 4(a)** in perspective, we have redone these calculations using the bcc phase as the reference for all pure elements. For this, we have performed another set of calculations for the three pure hcp elements Zr, Hf and Ti forcing a bcc crystal symmetry. The calculated lattice parameters thus obtained are $a_{\text{Ti}} = 3.252 \text{ \AA}$, $a_{\text{Zr}} = 3.573 \text{ \AA}$, and $a_{\text{Hf}} = 3.542 \text{ \AA}$ (and $a_{\text{Nb}} = 3.31 \text{ \AA}$, $a_{\text{Ta}} = 3.32 \text{ \AA}$ for the two last bcc elements). Using these relaxed lattice parameters, we recalculated the E_f of our alloys. **Figure 4(b)** shows the dependence of the energies $(\Delta H_{\text{form}})_x$ and $(\Delta G)_x$ on the Ti content calculated in this way. As the hcp elements are unstable in the bcc structure, formation energies are larger for these three pure elements, and the resulting formation energies of the alloys are all decreased. For $x = 0.0$ to 0.2 , the formation energies remained slightly positive, but for $x > 0.2$ it becomes still slightly negative. It must be noted that the bcc phase for the alloy becomes the most stable for all Ti compositions, which this time contrasts with the predictions from the $\overline{\text{Bo}} - \overline{\text{Md}}$ diagram.

Figure 4(a) shows the Gibbs free energy with the inclusion of configurational entropy is not enough to reach negative values at RT. The decrease in Gibbs free energy with Ti content is slightly smaller than the decrease in formation energy for bcc phase. Although, the formation energies remain slightly positive. In the context of HEA alloys, it was originally assumed that configurational entropy stabilizes the HEA phase by lowering the Gibbs free energy. The consensus is now more nuanced, as it has recently been shown that high configurational entropy is neither a sufficient nor a necessary condition for the formation of a single-phase solid solution [45–47]. In our case we have calculated the Gibbs free energy including the configurational entropy at 300 K using **Eq.3**.

Figure 4(c) shows the Gibbs free energy for the bcc and hcp phases at a temperature of 1000 K. At this temperature, the Gibbs free energy for the bcc structure is lower than that observed for the hcp structure. This suggests that the most stable bcc structure observed at high temperature need to transform into a hcp structure more stable at RT as alloys with $x > 0.5$ are

cooled down. Again, depending on the cooling rate, the hcp phase may well be trapped and remain metastable, which could lead to a duplex bcc-hcp structure for the corresponding alloys.

The fact that the formation energy remains positive, albeit slightly, while an HEA solid solution phase is observed in the experiments can be explained in several ways. First, a positive formation energy could indicate that the HEA phase is metastable at RT. Second, the presence of SROs could be associated with more favorable bonding, which would lower the formation energies (see previous section). Another explanation for this positive value for all Ti content x could be due to the coexisting phases at RT. Since our alloy consists of hcp and bcc elements - from the binary phase diagram [41] for atomic pairings, e.g., Ta-Hf, Ta-Zr, Nb-Hf and Nb-Zr - there is a miscibility gap at low temperature, which could be responsible for the increase in formation energy.

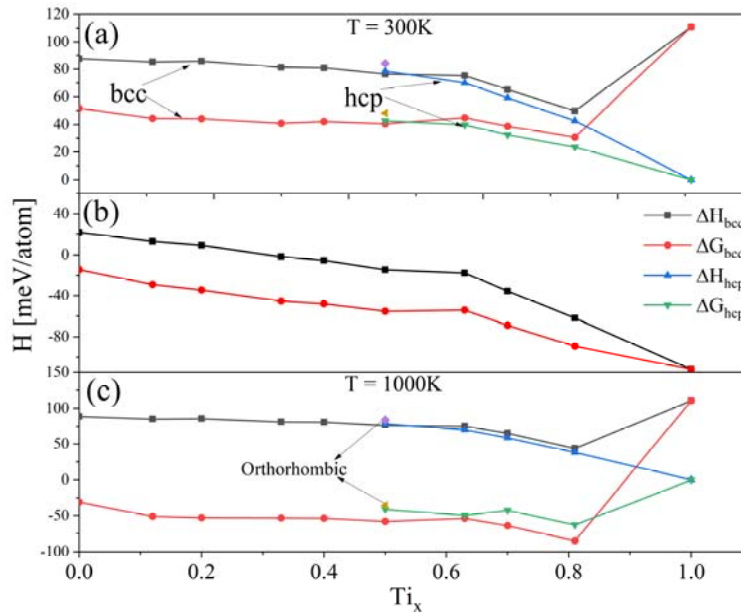


Figure 4: Calculated formation energy (ΔH) and Gibbs free energy (ΔG) of $Ti_x(HfNbTaZr)_{(1-x)/4}$ alloys using the reference state as **(a)** stable (bcc and hcp phases for all elements) and **(b)** unstable phase of the various elements composing our alloy (bcc structure for all elements). In **(a)** and **(b)** the Gibbs free energy is given at 300 K. Figure **(c)** is similar to **(a)** but the Gibbs free energy is now calculated at 1000 K using the stable phase for all elements as reference phase.

3.5. Elastic constants for bcc $\text{Ti}_x(\text{HfNbTaZr})_{(1-x)/4}$ alloys

Elastic constants can also be employed as an alternative criterion for evaluating the structural stability and mechanical properties of alloys. To calculate these properties, we used the strain energy approach to obtain the elastic tensor. Another approach would be to use the strain-stress approach as implemented in VASP to determine the full elastic tensor, but due to the large size of the system we resort to the former approach.

A strain up to 3% on the equilibrium structure was applied to produce eleven intermediate deformed structures, followed by relaxation of each atomic structure using the same settings as given in **Section 2**. To obtain the individual constants, a suitable choice of deformation tensor was applied to the relaxed equilibrium SQS supercell for all Ti content x . Here we focus on the bcc elastic properties and will limit calculations to $x \leq 0.5$, for which the bcc phase is unambiguously the most stable phase. More details of the strain tensor corresponding to the individual cubic elastic constants may be found in [48].

The calculated elastic constants of the alloy $\text{Ti}_x(\text{HfNbTaZr})_{(1-x)/4}$ are given in **Table 5**. These calculations were carried out for the atomic configuration corresponding to the lowest formation energy for each x . We checked the mechanical stability for these atomic configurations, and they all satisfy the basic condition, i.e., $C_{11} > C_{12}$, $C_{11} + 2C_{12} > 0$, and $C_{44} > 0$. A simple way to assess the relevance of the obtained elastic constant is the Zener anisotropy ratio A_z . The anisotropy is low in the quaternary alloy $A_z = 1.5$, and the Zener coefficient then increases from 1.5 to 2.6 when the Ti content is increased from $x = 0.2$ to 0.5. For the equimolar composition $x = 0.2$, the values calculated at 0 K agree well with macroscopic measurements from experiments [7]. The largest deviation of 15% is observed for C_{11} . For $x = 0.2$, Fazakas *et al.* have reported the elastic constants using the coherent potential approximation (CPA). The CPA approximation considers only the single point energy of the supercell and not the relaxed atomic structure. The elastic constants reported in that study are as follows: 160.2 GPa for C_{11} , 124.4 GPa for C_{12} , and 62.4 GPa for C_{44} [49]. Compared to the values in **Table 5**, we see that the values for C_{12} and C_{44} seem overestimated if structural relaxation is not considered. Thus, to obtain a good approximation, it is necessary to relax the SQS structure.

Table 5: Elastic constants C_{ij} (GPa) ,and Zener anisotropy A_z coefficient calculated with the bcc-SQS supercell for $\text{Ti}_x(\text{HfNbTaZr})_{(1-x)/4}$ alloys. The experimental value for the known composition is given in parentheses. For comparison, the elastic constants of bcc Ti are also given.

x	0.00	0.11	0.20([7])	0.33	0.40	0.50	1.0
C_{11}	161.6	155.0	156.0(172±6)	153.8	147.0	133.6	106.4
C_{12}	108.9	107.9	104.7(108)	100.4	99.9	105.1	110.5
C_{44}	42.1	45.8	38.6(28±1.5)	45.1	41.4	36.9	45.3
A_z	1.5	1.9	1.5(1.0)	1.7	1.9	2.6	-

From the elastic constants, it is instructive to calculate the isotropic bulk modulus B , shear modulus G , and Young's modulus E and examine the trend as the Ti content is varied. The shear modulus is obtained from the average of Voigt and Reuss expression as suggested by Hill [50]. **Figure 5** shows that B decreases monotonically when increasing the Ti content, while

G and E are constant for $Ti_x < 0.4$ and significantly decrease until $x = 0.5$. From these two quantities, the Pugh's ratio (B/G), can be used to estimate the brittle or ductile nature of the material. Materials that have a high B value and a low G value are generally ductile. Since for all x the B/G is > 1.75 , according to Pugh's ratio this suggests a ductile nature of the alloy. Ultimately, the nice agreement between our results and experimental and simulation works validates our methodology based on a large number of MCSQS realizations prior to the DFT simulations. Besides, the Ti content x in the range (0, 0.5) can be employed to slightly modulate the elastic properties of these alloys to meet the value targets for specific applications.

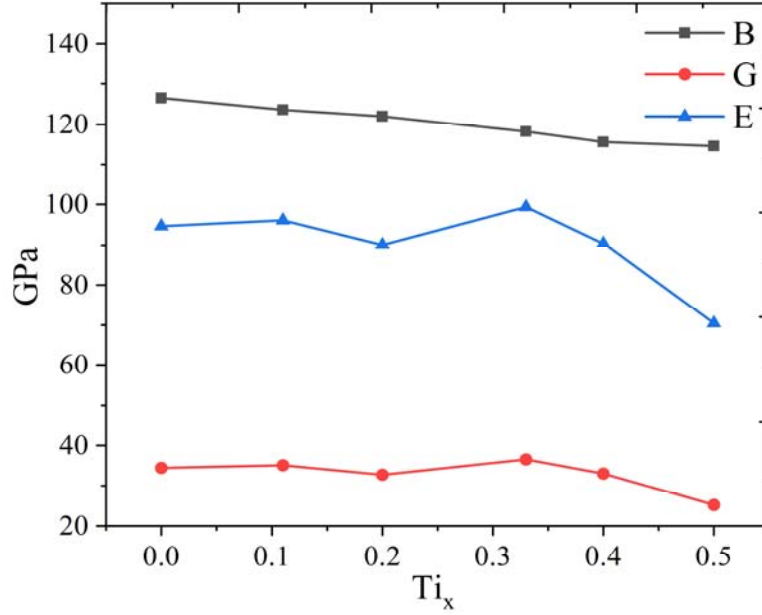


Figure 5: Isotropic elastic moduli for $Ti_x(HfNbTaZr)_{(1-x)/4}$ as a function of the Ti content x.

Conclusions

In this work we have studied the structure, phase stability and elastic behavior of $\text{Ti}_x(\text{HfNbTaZr})_{(1-x)/4}$ alloys as a function of the Ti content x . The atomistic structure, corresponding to the disordered structure of the HEA solid solution, was approximated using the MCSQS technique, and the atomic relaxation and energy calculations were performed using DFT calculations. The following results were obtained.

- We performed many SQS runs with different initial seeds and conducted a systematic sensitivity study on the number of NNs and the order of the many-body terms for Ti content x . In agreement with other studies, we found that the number of NN pairs has a stronger effect than higher bond orders to obtain an SQS configuration with a lower formation energy.
- Adjusting the Ti content x , which corresponds to the number of atoms and the size of the supercell, affects the formation energy of the system. An optimum of 8 NN p-shells is found for $x = 0.0$, 0.20 , and $x = 0.33$. For $x = 0.12$ and 0.50 , 6 NN was sufficient. This shows that the number of NN shells must be considered to obtain the lowest formation energy.
- The formation energy of alloys in bcc structure is slightly positive, but the value is smaller than the absolute value of the bulk energy of the individual element. The inclusion of configurational entropy does not lead to a negative Gibbs free energy at RT. A negative Gibbs free energy was obtained when the bcc phase was considered as the reference phase for all elements or when the configurational entropy was calculated at the elevated elaboration temperature. Thus, the bcc HEA phase observed experimentally for the equimolar alloy could be metastable or stabilized by SRO or vibrational entropy.
- We have proposed an original analysis of the short-range chemical ordering in the HfNbTaZr and TiHfNbTaZr systems based on a large number of MCSQS realizations and a corresponding DFT calculation for each of them. The average configuration from the large number of MCSQS realizations is a good approximation to the ideal random structure. The different configurations can then be sorted as a function of the associated formation energy, and correlations can be pursued.
- The chemical local ordering was then analyzed for the best, average, and worst sets of MCSQS as a function of formation energy. Somewhat simplistically, elements with identical crystallographic structure are typically favorable, while elements with different crystallographic structure are unfavorable and their presence is minimized in the best SQS sets. It would be interesting to see if this simple explanation can be applied to other HEA systems with elements of different crystallographic structure. The SRO in HfNbTaZr is mainly located on the 2nd NN shell, while in TiHfNbTaZr all the first three NN shells are involved. Few bond pairs are favorable in the quaternary system, and this could explain the weak global SRO in this system. The SRO appears to be present in both systems, although it is stronger in the quinary system. This SRO could help reduce the formation energy and justify the stability of the HEA solid solution.

- The content of Ti has various effects on the structure or properties of the $\text{Ti}_x(\text{HfNbTaZr})_{(1-x)/4}$ system. The average bcc lattice parameter and the formation energies decrease monotonically with the Ti content. When the Ti content exceeds 0.5, the hcp phase is the most stable phase. The orthorhombic structure-a third possible phase-is discarded when the configurational entropy term is considered. These results are consistent with the so-called $\overline{Bo} - \overline{Md}$ diagram, which was originally proposed to predict the phase stability of Ti alloys.
- The present work is qualitatively consistent with trends found in HEA systems and quantitatively consistent with the limited literature on this system. The average bcc lattice parameter and elastic constants agree with experimental values obtained for the equimolar alloy. The energy of formation is also in agreement with the results obtained for the equimolar alloy in [44].

Acknowledgments

We are grateful to XXX, Univ. Sorbonne, Paris Nord, Labex SEAM, ANR (Agence Nationale de la Recherche) and CGI (Commissariat à l'Investissement d'Avenir) for financing this work through Labex SEAM (Science and Engineering for Advanced Materials and devices), ANR-10-LABX-0096 and ANR-18-IDEX-0001. Further, we would like to thank Ing. Nicolas Greneche for HPC support, MAGI, Univ. Sorbonne Paris Nord and HPC resources.

References

- [1] N. Ma, S. Liu, W. Liu, L. Xie, D. Wei, L. Wang, L. Li, B. Zhao, Y. Wang, Research Progress of Titanium-Based High Entropy Alloy: Methods, Properties, and Applications, *Front Bioeng Biotechnol.* 8 (2020) 1303. <https://doi.org/10.3389/fbioe.2020.603522>.
- [2] S. Gurel, M.B. Yagci, D. Canadinc, G. Gerstein, B. Bal, H.J. Maier, Fracture behavior of novel biomedical Ti-based high entropy alloys under impact loading, *Materials Science and Engineering A.* 803 (2021) 140456. <https://doi.org/10.1016/j.msea.2020.140456>.
- [3] Y. Yuan, Y. Wu, Z. Yang, X. Liang, Z. Lei, H. Huang, H. Wang, X. Liu, K. An, W. Wu, Z. Lu, Formation, structure and properties of biocompatible TiZrHfNbTa high-entropy alloys, *Mater Res Lett.* 7 (2019) 225–231. <https://doi.org/10.1080/21663831.2019.1584592>.
- [4] M.C. Gao, C.S. Carney, N. Doğan, P.D. Jablonksi, J.A. Hawk, D.E. Alman, Design of Refractory High-Entropy Alloys, *JOM.* 67 (2015) 2653–2669. <https://doi.org/10.1007/s11837-015-1617-z>.
- [5] D.B. Miracle, O.N. Senkov, A critical review of high entropy alloys and related concepts, *Acta Mater.* 122 (2017) 448–511. <https://doi.org/10.1016/j.actamat.2016.08.081>.
- [6] Y. Ikeda, B. Grabowski, F. Körmann, Ab initio phase stabilities and mechanical properties of multicomponent alloys: A comprehensive review for high entropy alloys and compositionally complex alloys, *Mater Charact.* 147 (2019) 464–511. <https://doi.org/10.1016/j.matchar.2018.06.019>.
- [7] G. Dirras, L. Lilensten, P. Djemia, M. Laurent-Brocq, D. Tingaud, J.P. Couzinié, L. Perrière, T. Chauveau, I. Guillot, Elastic and plastic properties of as-cast equimolar TiHfZrTaNb high-entropy alloy, *Materials Science and Engineering A.* 654 (2016) 30–38. <https://doi.org/10.1016/j.msea.2015.12.017>.
- [8] O.N. Senkov, D.B. Miracle, K.J. Chaput, J.P. Couzinié, Development and exploration of refractory high entropy alloys - A review, *J Mater Res.* 33 (2018) 3092–3128. <https://doi.org/10.1557/jmr.2018.153>.
- [9] S. Gurel, M.B. Yagci, B. Bal, D. Canadinc, Corrosion behavior of novel Titanium-based high entropy alloys designed for medical implants, *Mater Chem Phys.* 254 (2020) 123377. <https://doi.org/10.1016/j.matchemphys.2020.123377>.

- [10] Y.Y. Zhao, Z.F. Lei, Z.P. Lu, J.C. Huang, T.G. Nieh, A simplified model connecting lattice distortion with friction stress of Nb-based equiatomic high-entropy alloys, *Mater Res Lett.* 7 (2019) 340–346. <https://doi.org/10.1080/21663831.2019.1610105>.
- [11] Y.C. Huang, Y.C. Lai, Y.H. Lin, S.K. Wu, A study on the severely cold-rolled and annealed quaternary equiatomic derivatives from quinary HfNbTaTiZr refractory high entropy alloy, *J Alloys Compd.* 855 (2021) 157404. <https://doi.org/10.1016/j.jallcom.2020.157404>.
- [12] S. Yin, J. Ding, M. Asta, R.O. Ritchie, Ab initio modeling of the energy landscape for screw dislocations in body-centered cubic high-entropy alloys, *NPJ Comput Mater.* 6 (2020). <https://doi.org/10.1038/s41524-020-00377-5>.
- [13] T. Kostiuchenko, F. Körmann, J. Neugebauer, A. Shapeev, Impact of lattice relaxations on phase transitions in a high-entropy alloy studied by machine-learning potentials, *NPJ Comput Mater.* 5 (2019). <https://doi.org/10.1038/s41524-019-0195-y>.
- [14] W. Feng, Y. Qi, S. Wang, Effects of short-range order on the magnetic and mechanical properties of FeCoNi(AlSi)_x high entropy alloys, *Metals (Basel)*. 7 (2017) 482. <https://doi.org/10.3390/met7110482>.
- [15] Z. Pei, R. Li, M.C. Gao, G.M. Stocks, Statistics of the NiCoCr medium-entropy alloy: Novel aspects of an old puzzle, *NPJ Comput Mater.* 6 (2020). <https://doi.org/10.1038/s41524-020-00389-1>.
- [16] D. Sobieraj, J.S. Wróbel, T. Rygier, K.J. Kurzydłowski, O. el Atwani, A. Devaraj, E. Martinez Saez, D. Nguyen-Manh, Chemical short-range order in derivative Cr-Ta-Ti-V-W high entropy alloys from the first-principles thermodynamic study, *Physical Chemistry Chemical Physics*. 22 (2020) 23929–23951. <https://doi.org/10.1039/d0cp03764h>.
- [17] A. Tamm, A. Aabloo, M. Klintonberg, M. Stocks, A. Caro, Atomic-scale properties of Ni-based FCC ternary, and quaternary alloys, *Acta Mater.* 99 (2015) 307–312. <https://doi.org/10.1016/j.actamat.2015.08.015>.
- [18] S. Yin, Y. Zuo, A. Abu-Odeh, H. Zheng, X.G. Li, J. Ding, S.P. Ong, M. Asta, R.O. Ritchie, Atomistic simulations of dislocation mobility in refractory high-entropy alloys and the effect of chemical short-range order, *Nat Commun.* 12 (2021). <https://doi.org/10.1038/s41467-021-25134-0>.
- [19] G. Kresse, J. Hafner, Ab initio molecular dynamics for liquid metals, *Phys Rev B.* 47 (1993) 558–561. <https://doi.org/10.1103/PhysRevB.47.558>.
- [20] G. Kresse, D. Joubert, From ultrasoft pseudopotentials to the projector augmented-wave method, *Phys Rev B.* 59 (1999) 1758–1775. <https://doi.org/10.1103/PhysRevB.59.1758>.
- [21] J.P. Perdew, K. Burke, M. Ernzerhof, Generalized Gradient Approximation Made Simple, *Phys Rev Lett.* 77 (1996) 3865–3868. <https://doi.org/10.1103/PhysRevLett.77.3865>.
- [22] M. Methfessel, A.T. Paxton, High-precision sampling for Brillouin-zone integration in metals, *Phys Rev B.* 40 (1989) 3616–3621. <https://doi.org/10.1103/PhysRevB.40.3616>.

- [23] H.J. Monkhorst, J.D. Pack, Special points for Brillouin-zone integrations, *Phys Rev B*. 13 (1976) 5188–5192. <https://doi.org/10.1103/PhysRevB.13.5188>.
- [24] C.W. Glass, A.R. Oganov, N. Hansen, USPEX-Evolutionary crystal structure prediction, *Comput Phys Commun.* (2006). <https://doi.org/10.1016/j.cpc.2006.07.020>.
- [25] P. Soven, Coherent-potential model of substitutional disordered alloys, *Physical Review*. 156 (1967) 809–813. <https://doi.org/10.1103/PhysRev.156.809>.
- [26] M.C. Gao, P. Gao, J.A. Hawk, L. Ouyang, D.E. Alman, M. Widom, Computational modeling of high-entropy alloys: Structures, thermodynamics and elasticity, *J Mater Res*. 32 (2017) 3627–3641. <https://doi.org/10.1557/jmr.2017.366>.
- [27] H. Song, F. Tian, Q.M. Hu, L. Vitos, Y. Wang, J. Shen, N. Chen, Local lattice distortion in high-entropy alloys, *Phys Rev Mater.* 1 (2017) 23404. <https://doi.org/10.1103/PhysRevMaterials.1.023404>.
- [28] A.E. Carlsson, P.A. Fedders, Maximum-entropy method for electronic properties of alloys, *Phys Rev B*. 34 (1986) 3567–3571. <https://doi.org/10.1103/PhysRevB.34.3567>.
- [29] A. van de Walle, P. Tiwary, M. de Jong, D.L. Olmsted, M. Asta, A. Dick, D. Shin, Y. Wang, L.-Q. Chen, Z.-K. Liu, Efficient stochastic generation of special quasirandom structures, *Calphad*. 42 (2013) 13–18. <https://doi.org/10.1016/j.calphad.2013.06.006>.
- [30] A. van de Walle, Multicomponent multisublattice alloys, nonconfigurational entropy and other additions to the Alloy Theoretic Automated Toolkit, *Calphad*. 33 (2009) 266–278. <https://doi.org/10.1016/j.calphad.2008.12.005>.
- [31] D. Alfè, PHON: A program to calculate phonons using the small displacement method, *Comput Phys Commun.* 180 (2009) 2622–2633. <https://doi.org/10.1016/j.cpc.2009.03.010>.
- [32] Z. Du, J. Zuo, N. Bao, M. Yang, G. Jiang, L. Zhang, Effect of Ta addition on the structural, thermodynamic and mechanical properties of CoCrFeNi high entropy alloys, *RSC Adv*. 9 (2019) 16447–16454. <https://doi.org/10.1039/c9ra03055g>.
- [33] F. Tian, D.Y. Lin, X. Gao, Y.F. Zhao, H.F. Song, A structural modeling approach to solid solutions based on the similar atomic environment, *Journal of Chemical Physics*. 153 (2020). <https://doi.org/10.1063/5.0014094>.
- [34] D. de Fontaine, The number of independent pair-correlation functions in multicomponent systems, *J Appl Crystallogr.* 4 (1971) 15–19. <https://doi.org/10.1107/s0021889871006174>.
- [35] S. Menon, G.D. Leines, J. Rogal, pycal: A python module for structural analysis of atomic environments, *J Open Source Softw.* 4 (2019) 1824. <https://doi.org/10.21105/JOSS.01824>.
- [36] M Moringa, N. Yukawa, T. Maya, Theoretical design of Titanium alloys, *Sixth World Conference on Titanium*. 1 (1988) 1601.

- [37] M. Abdel-Hady, K. Hinoshita, M. Morinaga, General approach to phase stability and elastic properties of β -type Ti-alloys using electronic parameters, *Scr Mater.* 55 (2006) 477–480. <https://doi.org/10.1016/j.scriptamat.2006.04.022>.
- [38] L. Lilensten, J.P. Couzinié, J. Bourgon, L. Perrière, G. Dirras, F. Prima, I. Guillot, Design and tensile properties of a bcc Ti-rich high-entropy alloy with transformation-induced plasticity, *Mater Res Lett.* 5 (2017) 110–116. <https://doi.org/10.1080/21663831.2016.1221861>.
- [39] O.N. Senkov, J.M. Scott, S. v. Senkova, D.B. Miracle, C.F. Woodward, Microstructure and room temperature properties of a high-entropy TaNbHfZrTi alloy, *J Alloys Compd.* 509 (2011) 6043–6048. <https://doi.org/10.1016/j.jallcom.2011.02.171>.
- [40] L.K. T.B. Massalski, H. Okamoto, P.R. Subramanian, *Binary Alloy Phase Diagrams*, 2nd ed., ASM International, Materials Park, OH, USA, 1990.
- [41] H. Okamoto, M.E. Schlesinger, E.M. Mueller, *Binary Alloy Phase Diagrams*, 2nd Edition - ASM International, (2016).
- [42] M. Chase, *JANAF Thermochemical Tables*, 3rd ed., 1985.
- [43] J.D. Cox, *CODATA Key Values for Thermodynamics*, Hemisphere Publ. Co., NY, 1989.
- [44] M.C. Gao, C. Niu, C. Jiang, D.L. Irving, Applications of special quasi-random structures to high-entropy alloys, *High-Entropy Alloys: Fundamentals and Applications.* (2016) 333–368. https://doi.org/10.1007/978-3-319-27013-5_10/FIGURES/12.
- [45] F. Otto, Y. Yang, H. Bei, E.P. George, Relative effects of enthalpy and entropy on the phase stability of equiatomic high-entropy alloys, *Acta Mater.* 61 (2013) 2628–2638. <https://doi.org/10.1016/j.actamat.2013.01.042>.
- [46] M. Laurent-Brocq, L. Perrière, R. Pirès, Y. Champion, From high entropy alloys to diluted multi-component alloys: Range of existence of a solid-solution, *Mater Des.* 103 (2016) 84–89. <https://doi.org/10.1016/j.matdes.2016.04.046>.
- [47] I.A. Tomilin, S.D. Kaloshkin, “High entropy alloys’-’semi-impossible” regular solid solutions?, *Materials Science and Technology (United Kingdom).* 31 (2015) 1231–1234. <https://doi.org/10.1179/1743284715Y.0000000028>.
- [48] R. Golesorkhtabar, P. Pavone, J. Spitaler, P. Puschnig, C. Draxl, ElaStic: A tool for calculating second-order elastic constants from first principles, *Comput Phys Commun.* 184 (2013) 1861–1873. <https://doi.org/10.1016/j.cpc.2013.03.010>.
- [49] E. Fazakas, V. Zadorozhnyy, L.K. Varga, A. Inoue, D. v. Louzguine-Luzgin, F. Tian, L. Vitos, Experimental and theoretical study of Ti₂₀Zr₂₀Hf₂₀Nb₂₀X₂₀ (X = v or Cr) refractory high-entropy alloys, *Int J Refract Metals Hard Mater.* 47 (2014) 131–138. <https://doi.org/10.1016/j.ijrmhm.2014.07.009>.
- [50] R. Hill, The elastic behaviour of a crystalline aggregate, *Proceedings of the Physical Society. Section A.* 65 (1952) 349–354. <https://doi.org/10.1088/0370-1298/65/5/307>.

